Rapid Prototyping J

Additive manufacturing of Aluminium alloy 2024 by laser powder bed fusion: Microstructural evolution, defects and mechanical properties

Journal:	*Rapid Prototyping Journal*
Manuscript ID	RPJ-10-2020-0241.R2
Manuscript Type:	Original Article
Keywords:	Additive Manufacturing (AM), Selective Laser Melting (SLM), Aluminium alloys, Solidification, Microstructure evolution

Additive manufacturing of Aluminium alloy 2024 by laser powder bed fusion: Microstructural evolution, defects and mechanical properties

Abstract

Purpose: The purpose of this study is to investigate the microstructural evolution of high strength 2024 Al-alloy prepared by the Laser- Powder Bed Fusion (L-PBF) additive manufacturing route. The high strength wrought Al-alloy has typically been unsuitable for AM due to its particular solidification characteristics such as hot cracking, porosity and columnar grain growth.

Design/methodology/approach: In this research work, samples were fabricated using L-PBF under various laser energy densities by varying laser power and scan speed. The microstructural features that developed during the solidification are correlated with operating laser parameters. In addition, Finite Element Modelling (FEM) was performed to understand the experimentally observed results.

Findings: Microstructure evolution and defect formation have been assessed, quantified, and correlated with operating laser parameters. Thermal behaviour of samples was predicted using FEM to support experimental observations. An optimised combination of intermediate laser power and scan speed produced the least defects. Higher energy density increased hot tearing along the columnar grain boundaries while lower energy density promoted void formation. From the quantitative results it is evident that with increasing energy density both the top surface and side wall roughness initially reduced till a minimum and then increased. Hardness and compressive strength were found to decrease with increasing power density due to stress relaxation from hot tearing.

Originality/value: This research work examined how L-PBF processing conditions influence the microstructure, defects, surface roughness and mechanical properties. Results indicates that complete elimination of solidification cracks can be only achieved by combining process optimisation and possible grain refining strategies.

Keywords: Additive Manufacturing (AM); Powder Bed Fusion (PBF); Aluminium alloys; Solidification; Microstructure evolution.

1. Introduction

Additive manufacturing (AM) is gaining widespread attention in the metal manufacturing industry for its ability to produce complex geometries and increased product customization for high quality structural components with improved functionality [1, 2]. This is particularly beneficial where conventional manufacturing reaches its limits in terms of design and manufacturing capabilities. Metallic AM systems can be classified as: (i) Powder Bed Fusion (PBF), (ii) Direct Energy Deposition (DED), and (iii) droplet-on-demand systems. PBF technologies include Selective Laser Melting (SLM) and Electron Beam Melting (EBM) [3]. All these varieties of AM processes carry similar attributes, and Laser powder bed fusion (L-PBF) is one of the most promising for metallic components with complex geometry as a laser is an ideal source for precise melting of metals and alloys [1, 4]. L-PBF has been successfully applied to different alloy systems including Ti-6Al-4V [5, 6], nickel-based superalloys [6-8], Al-Si-Mg alloys [9, 10], austenitic steels [11-13], high entropy alloys [14] and numerous other alloy systems [15-18].

Current research on L-PBF of Al-Alloys is predominantly focused on castable and weldable alloys, e.g., Al-10Si-Mg, Al-12Si-Mg, due to their process suitability compared to high-strength wrought Al-Alloys [19]. The major challenges in using a laser beam to melt Al-alloy powders in AM are [19, 20]: (i) much higher reflectivity (compared to other alloys) to the laser beam making laser melting of Al an energy inefficient process, (ii) Al powders readily develop an oxide (Al_2O_3) layer due to its high affinity to oxygen resulting in entrapment of oxide inclusions in the laser built components, and (iii) managing the thermal stresses developed in intricate geometry produced by L-PBF becomes even more crucial as they involve complex stress distribution and may further aggravate defect formation in the component. Furthermore, the repetitive melting and rapid cooling (up to 10^6 Ks^{-1}) [21] experienced by the material during L-PBF processing is significantly different from conventional casting and welding processes.

In L-PBF, alloys with a wide freezing range leads to hot cracking and volatilisation of elements, such as Zn and Mg, resulting in a turbulent melt-pool, excessive sputtering, and porosity formation during processing [20, 22].

Limited literature is available on the processing of high-strength Al-alloys through L-PBF, and specifically, on heat-treatable wrought alloys (2xx.x, 6xx.x and 7xx.x) [23-28]. Conventionally produced wrought Al-alloys possess ultimate tensile stress (UTS) in the range of 200 - 575 MPa and ductility of 3 - 20% depending on the deployed thermomechanical processing route during manufacturing [29]. On the other hand, besides the difficulties in L-PBF processing, the obtained mechanical properties of these alloys are an order of magnitude lower (25-40 MPa UTS and 0.3-0.7% ductility) than their conventionally manufactured counterparts due to build defects such as hot-cracking and voids [19]. Therefore, it is essential to understand the relationship between the defects and critical L-PBF processing parameters to produce defect free, high strength, and ductile parts.

In the current investigation, commercial high-strength heat treatable wrought Al 2024 alloy is used, which is widely deployed in aviation, aerospace, automotive, rail transit and several other fields due to its high specific strength, excellent fatigue properties and good damage tolerance [30-33]. Despite its wide range of applications, its feasibility as a material for AM (or L-PBF) is hardly reported. Therefore, the present study investigates L-PBF AM processing of 2024 Al alloy highlighting the microstructural evolution and defect formation, and their dependence on the process parameters. The influence of process parameters, and the resulting microstructural features, on the mechanical properties have been investigated to propose a suitable laser processing window. A finite element model (FEM) using Abaqus software was adopted to analyse the temperature development in the built component during the process to compliment the experimental results obtained.

2. Experimental Method

2.1 Alloy for additive manufacturing

Gas atomised 2024 Al alloy powder (Al-4.35Cu-1.50Mg-0.25Fe-0.60Mn-0.08Ti-0.05Cr, all compositions expressed in wt. %) from Carpenter Additive, UK with average particle size of 29 µm was used in this study. The powder was analysed using a Zeiss Sigma FE (Carl Zeiss Ltd, UK) scanning electron microscope (SEM). Figures 1(a) and (b) present the particle size distribution (PSD) of the alloy powder. PSD was calculated by measuring the diameters of the powder particles from the Secondary Electron SEM micrographs using ImageJ software (ImageJ, USA). More than 90 % of the particles were measured to be smaller than 50 µm.

2.2 Processing by L-PBF

For AM of samples, an M280 L-PBF 3D Printer was used (EOS, UK). Cubic (15 mm × 15 mm × 15 mm) and cylindrical (φ = 7 mm, h = 15 mm) specimens were fabricated for microstructural analysis and compression testing, respectively. Three samples produced for each condition to ensure reproducibility. The L-PBF machine is equipped with a Yb fibre laser of 400 W maximum power and beam spot size of 70 µm. Laser parameters used for building the samples are listed in Table 1. Hatch distance (distance between consecutive laser tracks within a layer) and the layer thickness (thickness between layers in the vertical Z direction) were kept constant at 170 µm and 20 µm, respectively. The energy density (E_d) was calculated using Equation 1, where P is laser power (W), V_s is scan velocity (mm/s) and h_d is hatch distance (mm).

$$E_d = \frac{P}{V_s \times h_d} \qquad (1)$$

A zigzag pattern was used as the scanning strategy and scanning direction was alternated by 90° for successive layers. The base plate (Al 2139) was maintained at a constant temperature of 200 °C through continuous heating to reduce the thermal gradient between the sample and

the base plate to minimise crack formation. An Argon atmosphere with less than 0.1 vol. % O_2 was maintained inside the build chamber to prevent oxidation of the specimens. Figure 1(c) shows the as-built cubes and cylinders.

2.3 Microstructure characterisation and quantification

To evaluate the microstructure along the build (vertical) direction and across the horizontal plane, samples were cut along the vertical and horizontal cross sections and prepared using standard metallographic procedure. Samples were compression mounted in a thermo-setting phenolic resin. Mounted samples were wet ground using P400 grit SiC paper and progressively polished using 9 µm, 3 µm and 1 µm diamond paste under 22N load. All samples went through a final polishing under 22N load using 0.06 µm colloidal silica suspension. The top surface and the side walls of the as-fabricated cubes were also investigated using a JSM 7800F SEM (JEOL Ltd, Japan) equipped with energy dispersive spectroscopy (EDS) and electron back-scattered diffraction (EBSD) detectors. For EBSD analysis, 0.2 µm step size with 20 kV accelerating voltage was used and samples were tilted 70° from horizontal to enhance EBSD signal. Quantitative analysis of defects in the samples was achieved by calculating the area fraction of cracks and voids by thresholding the optical images from the horizontal cross-sections using ImageJ software. The roughness of the top surface and the side walls were measured using an InfiniteFocus G5 confocal microscope (Bruker Alicona UK).

2.4 Assessment of mechanical behaviour

Microhardness measurements along the build and horizontal directions were carried out in a Wilson® VH1202 Vickers hardness tester (Buehler UK, UK) using 100 gF and dwell time of 10s. Compressiontesting was performed at room temperature on cylindrical samples using strainrate 0.005 /min., according to ASTM E9-19 [34]. Besides applying lubricant, thespecimen's dimension ratio (diameter/ length) was used 2.0 to avoid barrellingand buckling

effect. In addition to that, constant true strain rate to a strainlimit of ε = 0.5 is usually applied to avoid further barrelling. Through a compression test, we have measured maximum compressive strength, 0.2% offset yield strength (YS) and chord modules.

Table 1. Laser parameters used for manufacturing the samples and the surface roughness of top surface and side wall of manufactured cubes.

Sample ID	**Laser power, *P* (W)**	**Scan speed, v_s (mm/s)**	**Energy density, E_d(J/mm²)**
S1	350	1000	2.06
S2		800	2.58
S3		600	3.44
S4	300	1000	1.76
S5		800	2.2
S6		600	2.94
S7	250	1000	1.48
S8		800	1.84
S9		600	2.46

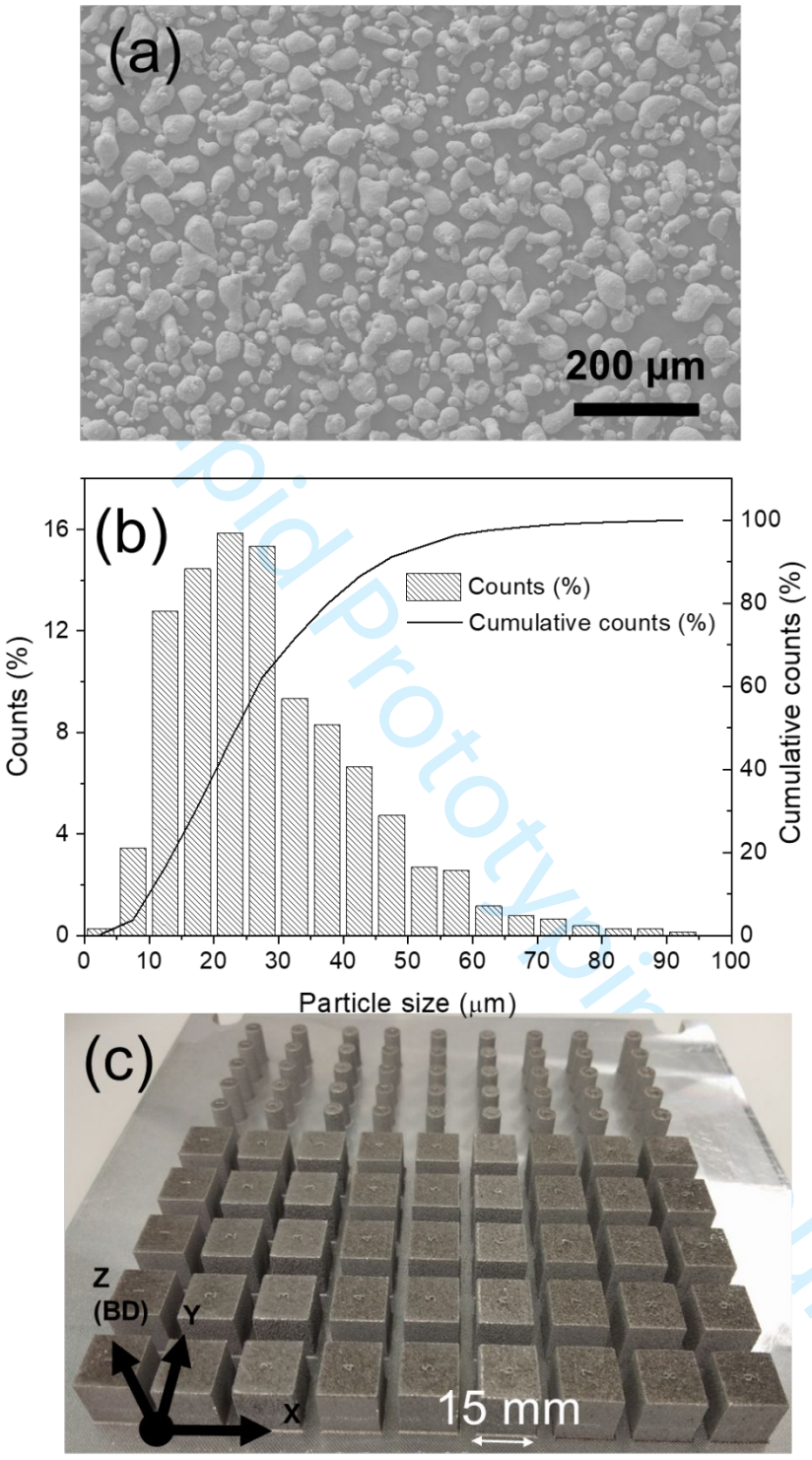

Figure 1: (a) Secondary electron SEM image of 2024 alloy gas atomised powder, (b) powder size distribution, average size is 29 µm, and (c) L-PBF printed cube (15 × 15 × 15 mm³) for microstructure analysis and cylinder (diameter = 7 mm, height = 15 mm) for compression testing.

3. Finite Element Model

For the finite element model, thermal conductivity [34, 35], and specific heat capacity [35] were taken from the literature and varied with temperature. Using the references outlined, Thermal conductivity (k) was taken to vary according to:

$$k = -5E\text{-}09T^4 + 7E\text{-}06T^3 - 0.0033T^2 + 0.9274T - 0.8253 \quad (2)$$

and Specific heat capacity (C_P) was taken to vary according to:

$$C_P = 5E\text{-}06T^3 - 0.0074T^2 + 3.9418T + 198.83 \quad (3)$$

Where T is the temperature in Kelvin. Values were inputted into the model up to 700 K.

Density was assumed to be 2,785 kg/m^3 at room temperature [36]. Latent heat was assumed to be 290,000 J/kg with a solidus of 773 K and a liquidus of 913K (calculated using Thermo-Calc software). These material properties were applied to both the base plate and the build section of the model.

The model consisted of a substrate measuring 20 x 100 x 100 mm^3, and a built cubic section of side length 15 mm. The cube was placed at the centre of one of the large faces of the substrate. The procedure to create the model outlined in the Abaqus manuals and in relevant publications was used [37-39]. To obtain the laser positional information, ReplicatorG software was then used to generate GCode files from a *.stl file exported from Abaqus. The Abaqus provided script (generateEventSeries.py) was then used to generate the required input files from the GCode file.

This resulted in a scan speed of 1 ms^{-1}, and a layer thickness of 20 μm, a hatch distance of 21 μm giving a total of 2.5 hrs (real time) to complete the build of the 15cm cube. This input data provided closest possible approximation of the original experiment as the original GCode was unavailable, and the finite element model was used to obtain qualitative data to help understand

the reasons for cracking during the build. The maximum time step in the model was limited to 2.0 sec to improve the resolution of temperature and stress during the build.

The substrate initial temperature was 473K. Cooling of the block was achieved through the application of a heat transfer coefficient of 18 $Wm^{-2}K^{-1}$ with a sink temperature of 473 K and an emissivity coefficient of 0.25 [37] with an ambient temperature of 473 K. Two laser powers were used for this finite element study (350 W and 250 W) with other laser parameters chosen to match the experimental values (Bead Height = 0.02 mm; Bead Width = 0.07 mm; "Energy Distribution" = "Concentrated"). 40,668 DC3D8 elements were used for the heat transfer model, which was found to be sufficient to accurately capture the thermal response. For the built part, a cubic element was used with an edge length of 0.5 mm.

4. Results and discussion

4.1 Defects formation: cracking, porosity, balling and agglomeration

Figure 2 shows the various internal and surface defects formed in the L-PBF cubes. These internal defects include hot tearing, hot shot and porosities (macro and micro). Hot tearing is identified as cracks, also known as hot cracks. Hot cracks are observed both inside and on the surface of the built components. Hot shots are generated due to insufficient molten metal filling the gaps arising out of contraction during solidification of build layers [40]. Macro pores form due to insufficient flow of the molten metal during solidification of the molten layer, whereas micro-pores are generated from *in-situ* release of gas bubbles [29]. The Al-Cu alloy system is susceptible to hot cracks due to its large freezing range [19]. Hot cracking tendency is directly related to the amount of eutectic liquid present during the later stages of solidification [41] and strong grain boundary segregation. Beyond a certain value, hot tearing decreases with increasing eutectic content as observed in the cast alloys (e.g. AlSi10Mg system) [41]. Quantification of total defect formation, and the average size and nature of the defects, is

presented in Figures 2(a) and (b). Figures 2(c) and (d) illustrates the defects developing in the sample built with higher laser power (350 W), showing that crack formation is more dominant than void formation at higher energy densities. In contrast to this, voids are the dominant defect in samples built under lower laser power (250 W) as shown in Figures 2(g)-(h), which reveals the presence of much larger voids than in 2(c) and (d). Sample S5, built with an intermediate power and scan speed, showed minimum total defects as shown in Figures 2(e)-(f).

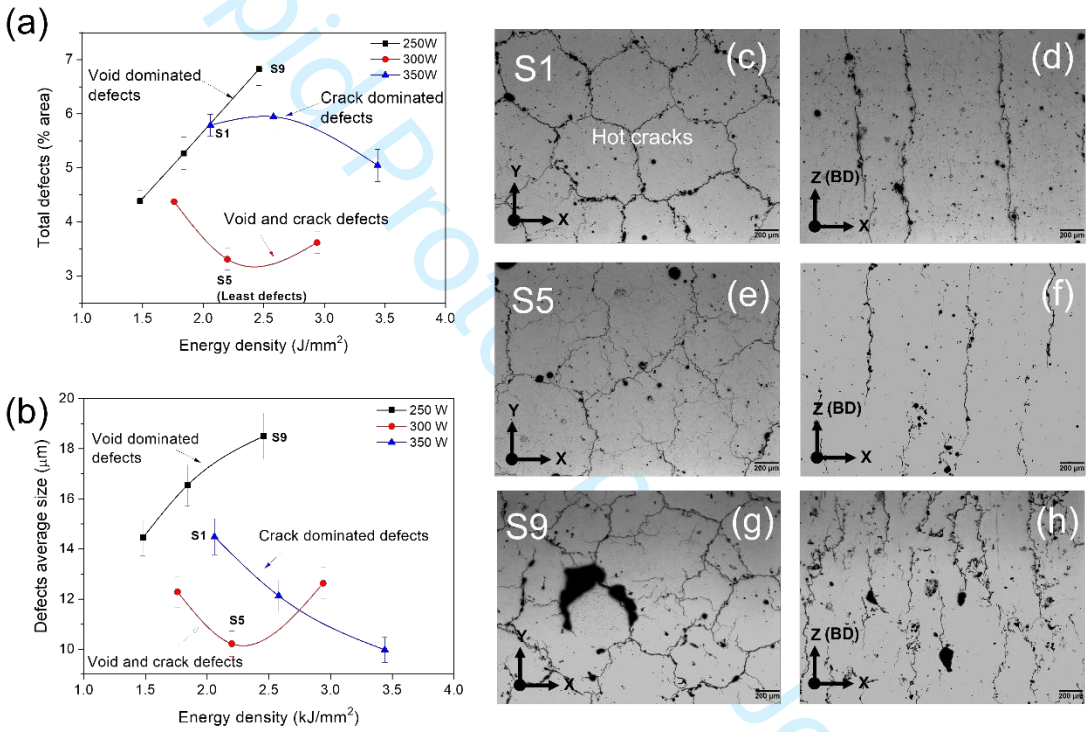

Figure 2: Quantitative analysis of defects with respect to the laser parameters at different E_d: (a) total area% of defects and (b) average size of defects (cracks and voids), where total defect represents the area fraction of both cracks and voids. Representative optical micrographs of sample S1(c) and (d); S5(e) and (f); and S9(g) and (h) showing distribution of defects in the horizontal and the vertical cross sections, respectively.

Figures 3(a)-(d) show various types of defects (e.g. hot tearing, voids, porosities, balling, etc.) observed in the samples. The nature of defects was observed to be dependent on the superheat of the melt pool. Higher input energy appears to increase the propensity of hot tearing.

However, total defects get balanced out due to minimisation of void formation as increased energy input provides sufficient melt fluidity, facilitating filling of shrinkage voids during solidification. Although the same energy input can be achieved with various combinations of laser power and scan speed, its interaction with material will be influenced by the individual laser parameters (power and scan speed). Therefore, defect formation, microstructure evolution and property evaluation will be discussed with respect to fundamental parameters (laser power and scan speed) along with respective energy densities.

Increased laser power (for a given scan speed) may increase the thermal gradient and promote a larger volume of superheated melt pool. Growth of columnar grains is enhanced and the liquid film between the large columnar grains is susceptible to form hot cracks along the grain boundaries, as seen in Figure 2(d). While increased laser power promotes the formation of cracks, it reduces the tendency of formation of hot shots.

Irregular voids or hot shots are caused by insufficient energy input causing incomplete melting of powder and incomplete filling of the voids and gaps (Rayleigh instability) [42]. Defects are found to be minimum for optimum laser power of 300 W at an intermediate energy input (S5) of 2.2 J/mm^2. Hot tearing is more prominent at higher power levels, whereas voids and hot shots are the prominent defects formed in samples built at lower power levels (see Figures 2(a) and (b)). This is due to insufficient superheat in the melt pool at low laser power, reducing melt fluidity and causing incomplete filling of shrinkage voids [43].

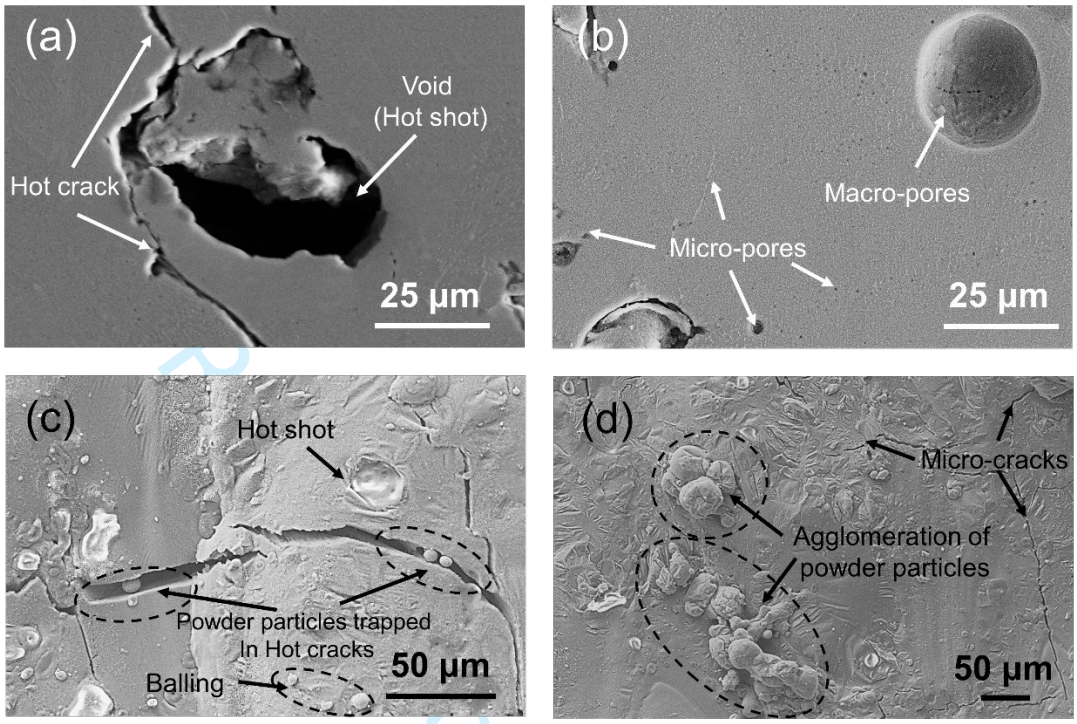

Figure 3: SEM micrographs showing various defects formed in the L-PBF samples (S9 for (a), (b) and (d), and S1 for (c)).

Besides internal defects, several surface defects could also be observed on the side walls and the top surface of the cubes. The micrographs from the top surface provide important information on the gradual development of defects in L-PBF printed cubes. Figures 3(c) and (d) show the surface defects on the final deposited layer of the cubes. Hot shots, cracks, balling and agglomeration of powders are observed on the surface. Balling and agglomerations are likely due to insufficient melting of the powder bed. However, balling and agglomerations could be re-melted during deposition of the next layer, but hot shots and cracks develop over multiple layers and that leads to accumulation of internal defects. Agglomeration of powders was also confirmed from the residual powder recollected from the chamber after the build was accomplished.

4.2 Microstructural evolution

EBSD analysis shows (Figure 4) the crystallographic texture present in the L-PBF produced cubes. Figure 4 presents the inverse pole figures (IPFs) of sample S5 (cube built with optimised laser parameters – minimum porosity and cracking defects) from the longitudinal (XZ plane) and the transverse cross section (XY plane). Columnar primary-Al grains grew along the building direction against the thermal gradient through epitaxial growth, which is very similar to microstructure reported in welding literature [44]. The sample exhibits <001>-fibre texture typical of directionally solidified structure in FCC alloys [45]. The average columnar grain size was 234 μm along the vertical (build) direction and 37 μm in the horizontal cross section. Figures 4(c) and (f) show that higher volume fractions of high angle grain boundaries (HAGBs) are oriented along the build direction and hot cracks were found to be present along these grain boundaries. EBSD micrographs were obtained from samples with different processing conditions to S5 but were found not to provide any new or additional information.

In addition, all samples exhibit cracks and these have been characterised carefully by detailed microscopy. In the welding literature three type of cracks are observed depending on the alloys and processing conditions [46]: (i) during solidification cracking is observed due to hot tearing, (ii) liquation type cracking is observed because of segregation of the solute elements in the grain boundary, and (iii) solid-state cracking is often observed because of the residual stresses generated during the welding. In the present work, we have used Thermo-Calc calculation to study solidification of the AA2024 alloy phase. Figure 5(a) clearly shows that AA2024 alloy has a long solidification range ~ 120 °C (from 640 °C to 520 °C), in comparison with the Al10SiMg alloy (~25 °C) making it vulnerable to cracking during AM. EDS spectra from the sample is presented in Figure 5(b) showing strong copper segregation along the grain boundaries. This Cu segregation in Cu at grain bounties occurs through successive solidification and melting events, accomplice by solid-state diffusion. This indicates the

presence of a Cu-rich liquid film at the HAGBs and suggests liquation type cracking, occurring during solidification, rather than during cooling of the solidified built samples. The long solidification range, solute segregation and the steep temperature gradient in L-PBF would create the right environment for the liquation at first, followed by hot-cracking up to a few mm in size.

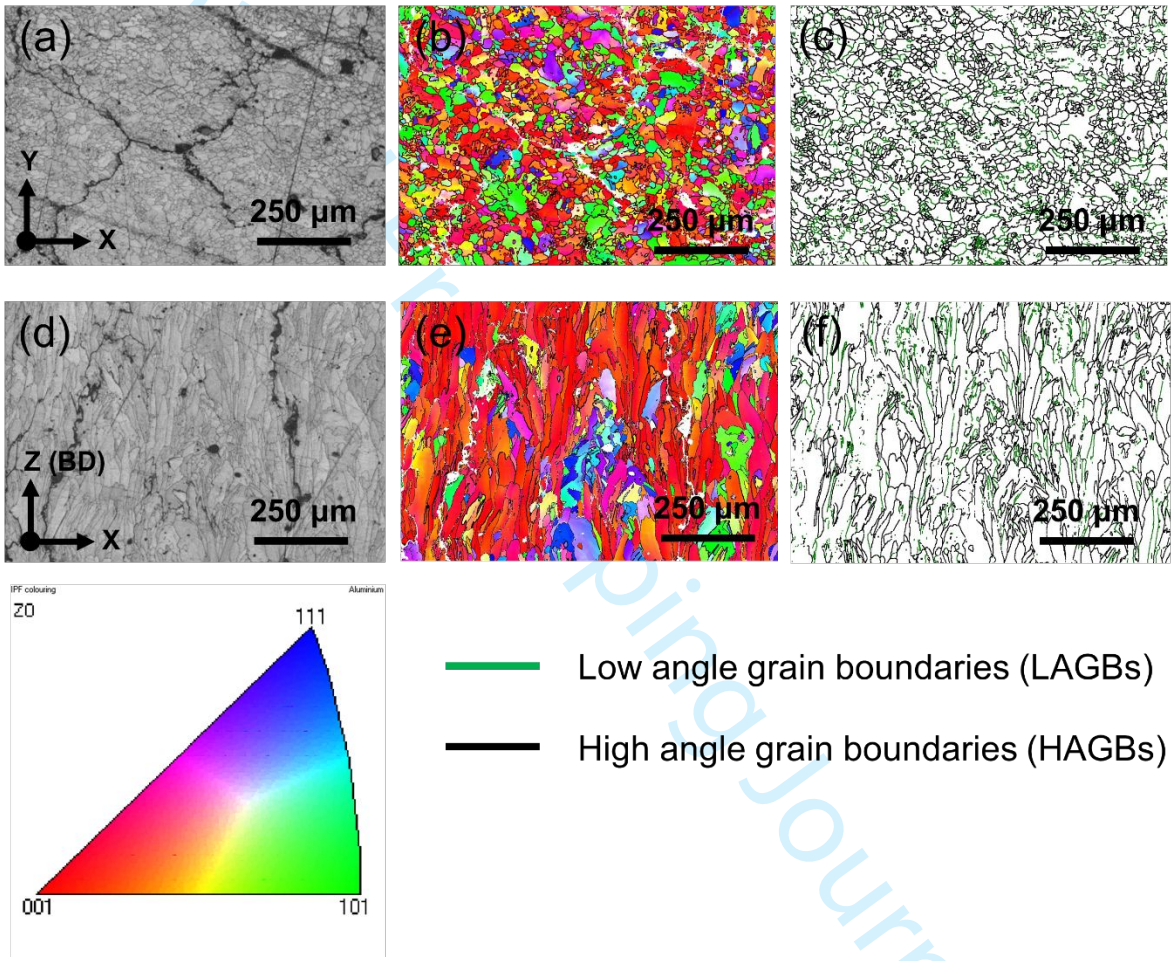

Figure 4: Representative micrographs showing grain structure and hot cracks along grain boundary: (a) to (c) plane of fabrication; (d) to (f) build direction. EBSD map in (b) and (e) showing directional growth of primary-Al grain along <001> direction.

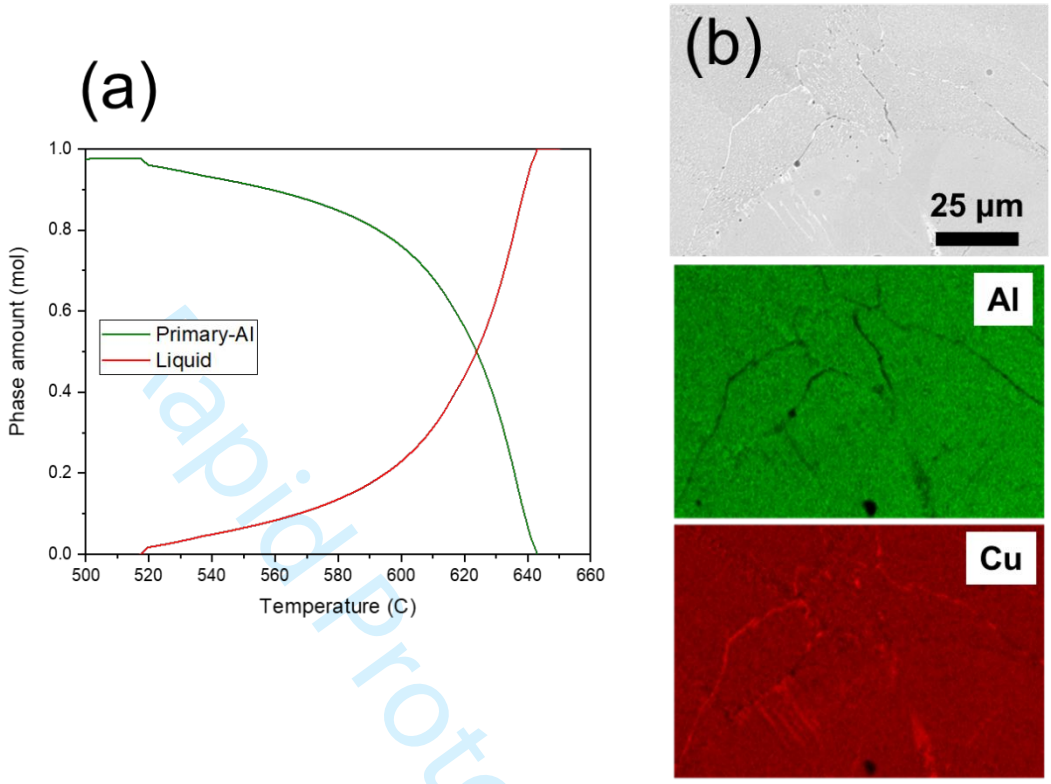

Figure 5: (a) AA2024 alloy Thermo-Calc calculated about the solidification range and (b) EDS spectra from the cracked columnar region in a sample. The grain boundary areas indicating strong segregation of Cu that is absent in the cracked regions.

4.3 Finite element analysis

For the finite element model, the origin is defined at the centre of the top face of the substrate where the material is added. The build takes place in the positive Z-direction replicating the experimental case. To observe temperature differences during the build, the following locations were chosen:

1) Centre of substrate face (0, 0, 0) – node 5154;
2) Centre of build (0, 0, 7.5) – node 23792;
3) Centre of built face (15, 0, 7.5) – node 1790;

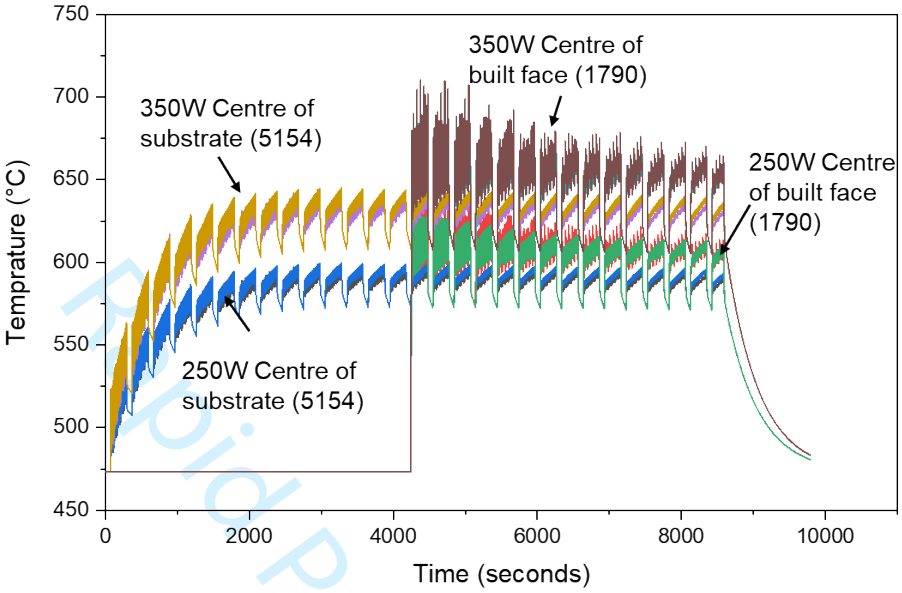

Figure 6: Abaqus predicted temperature profiles during build of 15 mm cube.

Figure 6 shows the predicted temperature profile at discrete points during the build. At the centre of the substrate face, the temperature is typically 50 K higher for the 350 W laser. Similarly, at the centre of a built face and the centre of the block, the temperature is typically 90 K higher for the 350 W laser, reaching over 720 K for the 350 W laser. This increase in temperature for the 350 W laser extends the length of time that the metal spends in the brittle temperature region during cooling (above 700 K), thereby increasing the propensity to cracking due to the hot shortness properties of this alloy [47, 48]. Increasing the cooling rate after deposition may help to reduce cracking [49]. This thermal prediction supports the observation from EDS analysis (Figure 5) suggesting hot tearing contributed to cracking observed in the samples.

4.4 Surface roughness and mechanical performance in the as-fabricated microstructures

Mechanical performance of structural components significantly depends on their surface finish. Figure 7 presents the average roughness (Ra) and the vertical distance from the highest peak to

the lowest trough (Rz) of the top surface and the side wall of the built cubes as a function of laser power, scan speed, and energy density (E_d). Figures 7(a) and (b) show that the top surface and the side wall roughness is strongly dependent on the applied laser power. It is predominantly affected by balling phenomenon. Under increased laser power, the heat input is higher and the enhanced melt fluidity results in a smoother surface. Figures 7(c) and (d) show increasing scan speed results in higher roughness of the top surface , however, no consistent trend is observed for the side wall. Slower scan speed facilitates longer interaction time between the energy source (laser) and the powder bed. At the lowest laser power and speed, surface roughness is highest as this power level is probably insufficient to fully melt the powders and not significantly affected by the scan speed. Higher heat input at higher laser power (P = 350 W) leads to more neighbouring powder particles being melting on to the build surface, thus reduce surface roughness. Similarly, at slower scan speed the laser beam has more interaction time with the surrounding powder particles. This facilitates more particles to become fused to the build surface, resulting in reduced surface roughness. Agglomeration of neighbouring powders into the build at the side wall results in greater roughness than the top surface at any laser power and most scan speeds. Furthermore, surface roughness as a function of E_d are show in Figures 7(e) and (f). From the quantitative results it is evident that with increasing E_d both the top surface and side wall roughness initially reduced till a minimum and then increased. Increasing E_d from 1.5 to 2.5 J/mm^2 enlarges the melt pool increasing molten liquid fluidity. This significantly reduced any balling effect leading to a reduction in the surface roughness from 20 to 5 μm for the top surface and 25 to 12 μm for the side wall. Similar observation has also been made for the Rz value. Further increasing E_d from 2.5 to 3.5 J/mm^2 probably leads toan unstable melt pool contributing an increase in surface roughness. This is consistent with previous observation of initial decrease in the surface roughness with energy density followed by an increase beyond a critical limit [50].

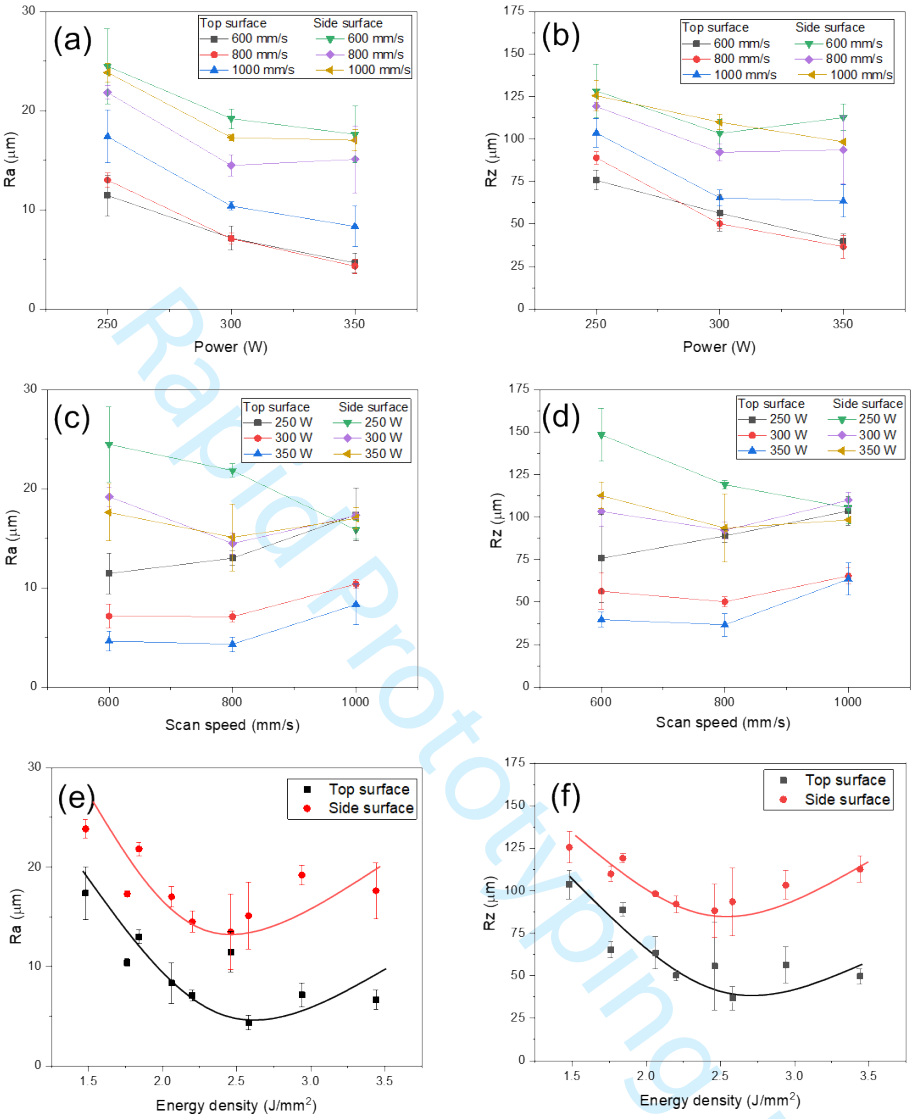

Figure 7: Variation in surface roughness of the top and side surface with (a) and (b) laser power, (c) and (d) scan speed, and (e) and (f) energy density (E_d). Ra is the average distance between the peaks and the troughs and Rz represents the vertical distance from the highest peak to the lowest trough.

Figure 8 presents the mechanical properties of the L-PBF samples built under different processing conditions. From Figure 8(a) it can be inferred that average hardness is strongly dependent on laser power, with a decrease in average hardness observed with increasing laser power. Figure 8(b) shows an increase in hardness corresponding to an increase in the scan

speed. In terms of Ed, average hardness decreased with an increase in Ed at a specific laser power or scan speed. Although residual stresses are expected to increase with an increase in energy input (increased power or decreased scan speed) leading to higher hardness, present results suggest that proportionate hot cracking at high energy inputs leads to 'stress relaxation' in the samples leading to reduced hardness observed in figure 8(c). Figure 8(d) represents the engineering compressive stress-strain curves for samples built with representative energy densities and figures 8(e) and (f) summarises the compressive strength, 0.2% offset yield strength (YS) and chord modules as a function of Ed. Compression test results displayed a decreasing compressive strength and YS with increasing Ed, however, higher chord modulus was measured at intermediate E_d level (between 2 to 2.9 J/mm^2) (Figure 8 (e)). The compressive strength was found to decrease with increased E_d due to the higher defect concentration in the samples built under increased E_d. We attribute the large difference observed in mechanical property mainly to the defects such as crack, porosity and surface roughness rather than any grain refinement (Hall-Petch) effect. After compression test, samples were examined under SEM (Figure 8(g)) and shows further propagation of existing cracks as well as new cracks appearing in the regions of Cu segregation at the grain boundaries. The results revels that complete elimination of cracking in high strength 2xxx alloy also requires better understanding of solute segregation in additive manufacturing to develop strategies to counter cracking.

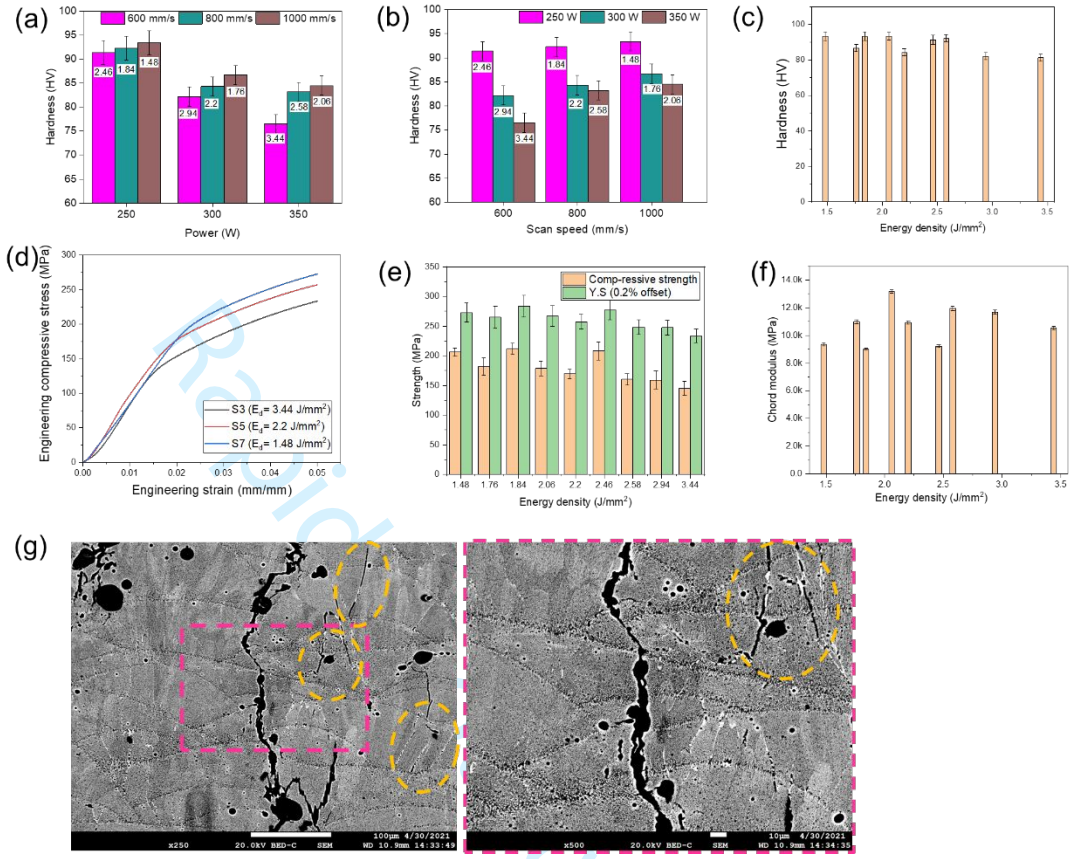

Figure 8: Microhardness of built specimen as a function of (a) laser power, (b) scan speed, and (c) energy density (E_d); E_d, is represented by the numerals in each bar of respective sample in (a) and (b). Representative engineering stress-strain curves obtained from compression testing are presented in (d), compressive strength, yield strength -0.2% off set (Y.S) and chord modules as function of E_d are presented in (e) and (f); and representative microstructure of tested sample (in build direction) shown crack opening and new cracks formation on Cu segregated grain boundary.

5. Conclusions

Microstructure and defects formed in Al-Cu (2024) alloy samples fabricated by L-PBF AM has been examined under different processing conditions. The following specific conclusions can be drawn from this work:

1. The columnar growth of primary-Al along the build direction and formation of internal and surface defects, such as hot cracking, hot shots, porosities, balling and powder agglomeration.
2. Samples produced using higher E_d showed increased hot-cracking, predominantly along the columnar grain boundaries, whereas samples produced at lower E_d showed increased numbers of voids and hot shots. Minimum defect formation (in terms of both size and volume) was observed at an optimum combination of intermediate laser power (300 W) and scan speed (800 mm/s) with a resulting E_d of 2.2 J/mm^2. The increased cracking observed under higher laser power appears to be contributed by increased metal temperature leading to brittle properties, as predicted using finite element analysis and verified through microstructural observations.
3. Surface roughness of samples was found to depend on the laser parameters. Higher power and energy density (2.5 J/mm^2) promote smoother surface by enlarging melt pool and subsequently increase molten liquid fluidity. However, beyond the critical limit (2.5 J/mm^2), led to an unstable melt pool contributing an increase in surface roughness.
4. Hardness was found to decrease with increased laser power and decreased scan speed due to 'stress relaxation' associated with hot-cracking under increased energy input. Ultimate compressive stress was also found to decrease with increased energy density.

References

[1] D.D. Gu, W. Meiners, K. Wissenbach, R. Poprawe, Laser additive manufacturing of metallic components: materials, processes and mechanisms, International Materials Reviews 57(3) (2012) 133-164.
[2] D. Herzog, V. Seyda, E. Wycisk, C. Emmelmann, Additive manufacturing of metals, Acta Materialia 117 (2016) 371-392.
[3] W.E. Frazier, Metal Additive Manufacturing: A Review, Journal of Materials Engineering and Performance 23(6) (2014) 1917-1928.
[4] Psychosis and schizophrenia in adults: prevention and management, NICE guideline [CG178] (2014).
[5] D. Agius, K.I. Kourousis, C. Wallbrink, A Review of the As-Built SLM Ti-6Al-4V Mechanical Properties towards Achieving Fatigue Resistant Designs, Metals and Materials International 8 (2018) 75.

[6] T. DebRoy, H.L. Wei, J.S. Zuback, T. Mukherjee, J.W. Elmer, J.O. Milewski, A.M. Beese, A. Wilson-Heid, A. De, W. Zhang, Additive manufacturing of metallic components – Process, structure and properties, Progress in Materials Science 92 (2018) 112-224.
[7] K.N. Amato, S.M. Gaytan, L.E. Murr, E. Martinez, P.W. Shindo, J. Hernandez, S. Collins, F. Medina, Microstructures and mechanical behavior of Inconel 718 fabricated by selective laser melting, Acta Materialia 60(5) (2012) 2229-2239.
[8] Z. Wang, K. Guan, M. Gao, X. Li, X. Chen, X. Zeng, The microstructure and mechanical properties of deposited-IN718 by selective laser melting, Journal of Alloys and Compounds 513 (2012) 518-523.
[9] K. Kempen, L. Thijs, J. Van Humbeeck, J.P. Kruth, Mechanical Properties of AlSi10Mg Produced by Selective Laser Melting, Physics Procedia 39 (2012) 439-446.
[10] N. Read, W. Wang, K. Essa, M.M. Attallah, Selective laser melting of AlSi10Mg alloy: Process optimisation and mechanical properties development, Materials & Design (1980-2015) 65 (2015) 417-424.
[11] J. Suryawanshi, K.G. Prashanth, U. Ramamurty, Mechanical behavior of selective laser melted 316L stainless steel, Materials Science and Engineering: A 696 (2017) 113-121.
[12] P. Bajaj, A. Hariharan, A. Kini, P. Kürnsteiner, D. Raabe, E.A. Jägle, Steels in additive manufacturing: A review of their microstructure and properties, Materials Science and Engineering: A 772 (2020) 138633.
[13] F. Abe, K. Osakada, M. Shiomi, K. Uematsu, M. Matsumoto, The manufacturing of hard tools from metallic powders by selective laser melting, Journal of Materials Processing Technology 111(1) (2001) 210-213.
[14] Y. Brif, M. Thomas, I. Todd, The use of high-entropy alloys in additive manufacturing, Scripta Materialia 99 (2015) 93-96.
[15] W. Xiong, L. Hao, Y. Li, D. Tang, Q. Cui, Z. Feng, C. Yan, Effect of selective laser melting parameters on morphology, microstructure, densification and mechanical properties of supersaturated silver alloy, Materials & Design 170 (2019) 107697.
[16] H. Zhang, H. Zhu, T. Qi, Z. Hu, X. Zeng, Selective laser melting of high strength Al–Cu–Mg alloys: Processing, microstructure and mechanical properties, Materials Science and Engineering: A 656 (2016) 47-54.
[17] A. Iveković, N. Omidvari, B. Vrancken, K. Lietaert, L. Thijs, K. Vanmeensel, J. Vleugels, J.-P. Kruth, Selective laser melting of tungsten and tungsten alloys, International Journal of Refractory Metals and Hard Materials 72 (2018) 27-32.
[18] V. Manakari, G. Parande, M. Gupta, Selective Laser Melting of Magnesium and Magnesium Alloy Powders: A Review, Metals 7 (2017) 2.
[19] N.T. Aboulkhair, M. Simonelli, L. Parry, I. Ashcroft, C. Tuck, R. Hague, 3D printing of Aluminium alloys: Additive Manufacturing of Aluminium alloys using selective laser melting, Progress in Materials Science 106 (2019) 100578.
[20] W.E. King, A.T. Anderson, R.M. Ferencz, N.E. Hodge, C. Kamath, S.A. Khairallah, A.M. Rubenchik, Laser powder bed fusion additive manufacturing of metals; physics, computational, and materials challenges, Applied Physics Reviews 2(4) (2015) 041304.
[21] L. Qian, J. Mei, J. Liang, X. Wu, Influence of position and laser power on thermal history and microstructure of direct laser fabricated Ti–6Al–4V samples, Materials Science and Technology 21(5) (2005) 597-605.
[22] S.A.M. Tofail, E.P. Koumoulos, A. Bandyopadhyay, S. Bose, L. O'Donoghue, C. Charitidis, Additive manufacturing: scientific and technological challenges, market uptake and opportunities, Materials Today 21(1) (2018) 22-37.
[23] B. Ahuja, M. Karg, K.Y. Nagulin, M. Schmidt, Fabrication and Characterization of High Strength Al-Cu Alloys Processed Using Laser Beam Melting in Metal Powder Bed, Physics Procedia 56 (2014) 135-146.
[24] R. Casati, J.N. Lemke, A.Z. Alarcon, M. Vedani, Aging Behavior of High-Strength Al Alloy 2618 Produced by Selective Laser Melting, Metallurgical and Materials Transactions A 48(2) (2017) 575-579.

[25] S. Dadbakhsh, R. Mertens, K. Vanmeensel, J. Vleugels, J.V. Humbeeck, J.-P. Kruth, In situ alloying and reinforcing of Al6061 during selective laser melting, Procedia CIRP 74 (2018) 39-43.
[26] D. Carluccio, M.J. Bermingham, Y. Zhang, D.H. StJohn, K. Yang, P.A. Rometsch, X. Wu, M.S. Dargusch, Grain refinement of laser remelted Al-7Si and 6061 aluminium alloys with Tibor® and scandium additions, Journal of Manufacturing Processes 35 (2018) 715-720.
[27] M.L. Montero-Sistiaga, R. Mertens, B. Vrancken, X. Wang, B. Van Hooreweder, J.-P. Kruth, J. Van Humbeeck, Changing the alloy composition of Al7075 for better processability by selective laser melting, Journal of Materials Processing Technology 238 (2016) 437-445.
[28] S. Sun, P. Liu, J. Hu, C. Hong, X. Qiao, S. Liu, R. Zhang, C. Wu, Effect of solid solution plus double aging on microstructural characterization of 7075 Al alloys fabricated by selective laser melting (SLM), Optics & Laser Technology 114 (2019) 158-163.
[29] J. Davis, ASM Specialty Handbook: Aluminum and Aluminum Alloys, ASM International (1993).
[30] T. Gu, B. Chen, C. Tan, J. Feng, Microstructure evolution and mechanical properties of laser additive manufacturing of high strength Al-Cu-Mg alloy, Optics & Laser Technology 112 (2019) 140-150.
[31] P. Wang, C. Gammer, F. Brenne, K.G. Prashanth, R.G. Mendes, M.H. Rümmeli, T. Gemming, J. Eckert, S. Scudino, Microstructure and mechanical properties of a heat-treatable Al-3.5Cu-1.5Mg-1Si alloy produced by selective laser melting, Materials Science and Engineering: A 711 (2018) 562-570.
[32] E.A. Starke, J.T. Staley, Application of modern aluminum alloys to aircraft, Progress in Aerospace Sciences 32(2) (1996) 131-172.
[33] N.D. Alexopoulos, Z. Velonaki, C.I. Stergiou, S.K. Kourkoulis, Effect of ageing on precipitation kinetics, tensile and work hardening behavior of Al-Cu-Mg (2024) alloy, Materials Science and Engineering: A 700 (2017) 457-467.
[34] W.J.H. R.L. Powell, and H.M. Roder, Journal of Applied Physics 31(3) (1960) 496.
[35] H.W.D. C.F. Lucks, Thermal Properties of 13 Metals, ASTM, Special Technical Publication No. 2271958.
[36] MIL-HDBK-5H, (1998) 3-68.
[37] X. Song, S. Feih, W. Zhai, C.-N. Sun, F. Li, R. Maiti, J. Wei, Y. Yang, V. Oancea, L.R. Brandt, A.M. Korsunsky, Advances in additive manufacturing process simulation: Residual stresses and distortion predictions in complex metallic components, Materials and Design (2020).
[38] E.R. Denlinger, J.C. Heigel, P. Michaleris, T.A. Palmer, Effect of inter-layer dwell time on distortion and residual stress in additive manufacturing of titanium and nickel alloys, Journal of Materials Processing Technology 215 (2015) 123-131.
[39] E.R. Denlinger, P. Michaleris, Effect of stress relaxation on distortion in additive manufacturing process modeling, Additive Manufacturing 12 (2016) 51-59.
[40] N.T. Aboulkhair, N.M. Everitt, I. Ashcroft, C. Tuck, Reducing porosity in AlSi10Mg parts processed by selective laser melting, Additive Manufacturing 1-4 (2014) 77-86.
[41] S. Li, D. Apelian, Hot Tearing of Aluminum Alloys, International Journal of Metalcasting 5(1) (2011) 23-40.
[42] R. Martinez, I. Todd, K. Mumtaz, In situ alloying of elemental Al-Cu12 feedstock using selective laser melting, Virtual and Physical Prototyping 14(3) (2019) 242-252.
[43] S. Coeck, M. Bisht, J. Plas, F. Verbist, Prediction of lack of fusion porosity in selective laser melting based on melt pool monitoring data, Additive Manufacturing 25 (2019) 347-356.
[44] M. Miyagi, Y. Kawahito, H. Wang, H. Kawakami, T. Shoubu, M. Tsukamoto, X-ray phase contrast observation of solidification and hot crack propagation in laser spot welding of aluminum alloy, Optics express 26 (2018) 22626.
[45] P. Kontis, E. Chauvet, Z. Peng, J. He, A.K. da Silva, D. Raabe, C. Tassin, J.-J. Blandin, S. Abed, R. Dendievel, B. Gault, G. Martin, Atomic-scale grain boundary engineering to overcome hot-cracking in additively-manufactured superalloys, Acta Materialia 177 (2019) 209-221.
[46] S. Kou, Library, MRS Bulletin 28(9) (2003) 674-675.

[47] N.K. Hiroshi Tamura, Shozo Ochiai, Yasunori Katagiri, Cracking study of aluminum alloys by the variabletensile strain hot cracking test, Transaction of the Japan Welding Society 8(2) (1977) 63-69.
[48] F.M.G. M. Sheikhi, H. Assadi, Prediction of solidification cracking in pulsed laser welding of 2024aluminum alloy, Acta Materialia 82 (2015) 491-502.
[49] Q.S. Xitang Tian, Preventing welding hot cracking by welding with an intensive trailing cooler, Journal of Materials Processing Technology 97 (2000) 30-34.
[50] X. Yan, C. Chang, D. Dong, S. Gao, W. Ma, M. Liu, H. Liao, S. Yin, Microstructure and mechanical properties of pure copper manufactured by selective laser melting, Materials Science and Engineering: A 789 (2020) 139615.

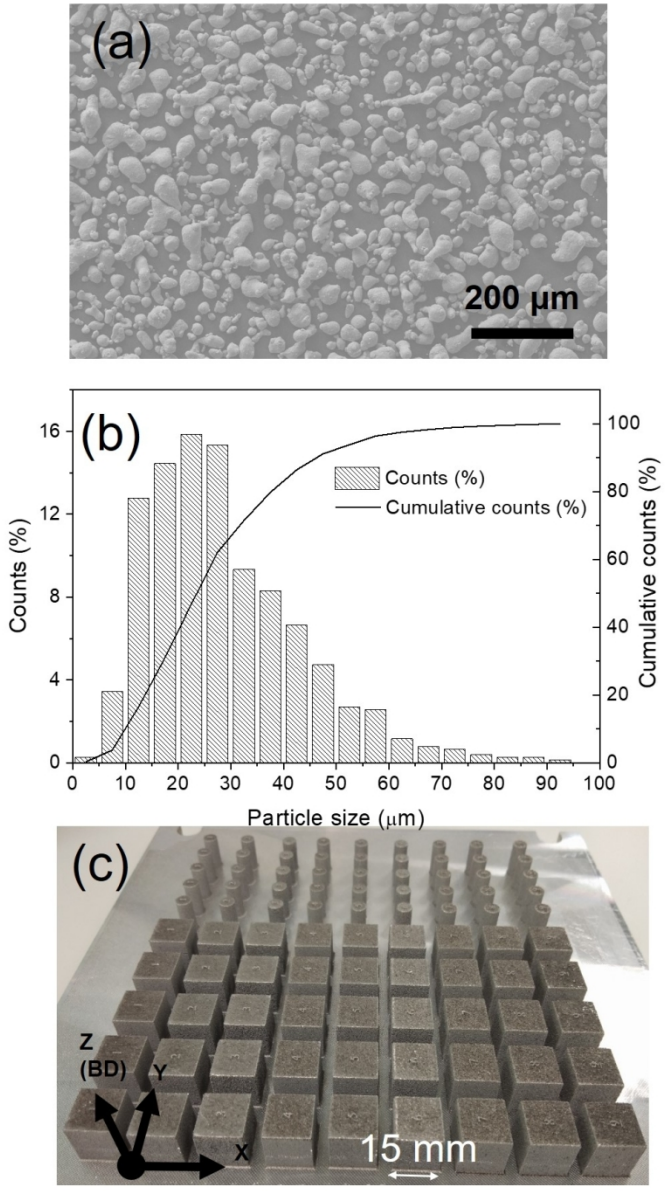

Figure 1: (a) Secondary electron SEM image of 2024 alloy gas atomised powder, (b) powder size distribution, average size is 29 µm, and (c) L-PBF printed cube (15 × 15 × 15 mm3) for microstructure analysis and cylinder (diameter = 7 mm, height = 15 mm) for compression testing.

177x302mm (150 x 150 DPI)

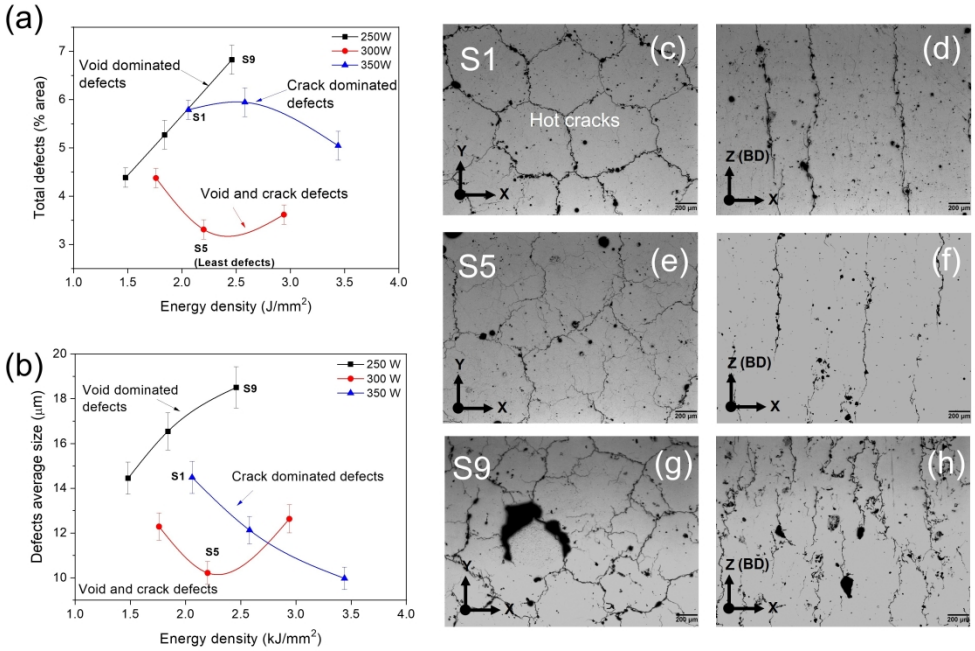

Figure 2: Quantitative analysis of defects with respect to the laser parameters at different Ed: (a) total area% of defects and (b) average size of defects (cracks and voids), where total defect represents the area fraction of both cracks and voids. Representative optical micrographs of sample S1(c) and (d); S5(e) and (f); and S9(g) and (h) showing distribution of defects in the horizontal and the vertical cross sections, respectively.

662x444mm (150 x 150 DPI)

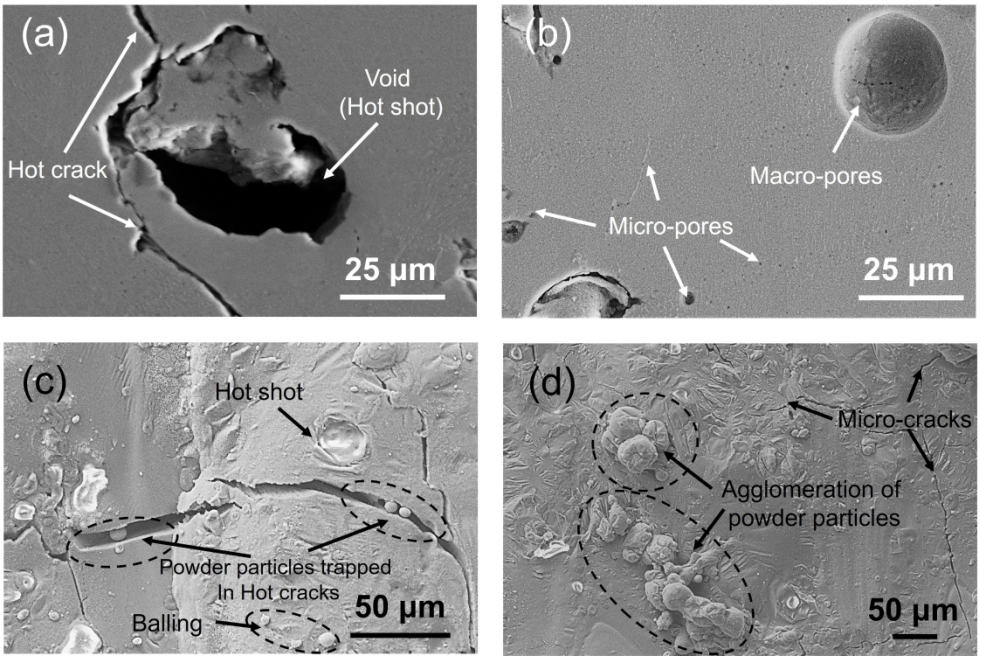

Figure 3: SEM micrographs showing various defects formed in the L-PBF samples (S9 for (a), (b) and (d), and S1 for (c)).

535x353mm (150 x 150 DPI)

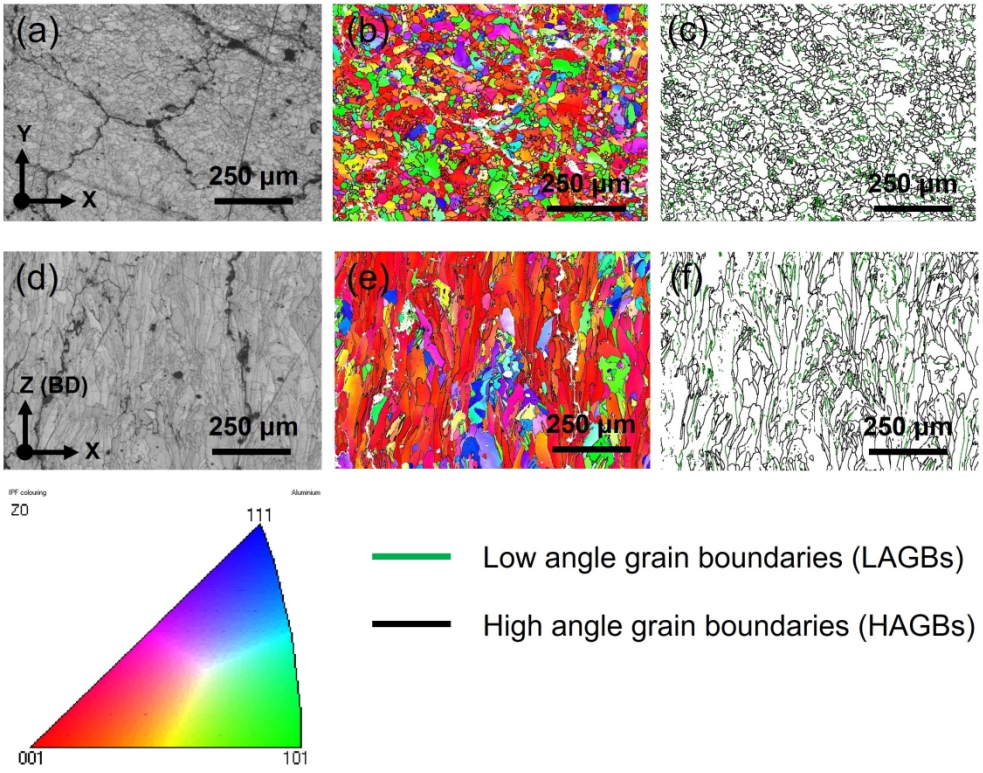

Figure 4: Representative micrographs showing grain structure and hot cracks along grain boundary: (a) to (c) plane of fabrication; (d) to (f) build direction. EBSD map in (b) and (e) showing directional growth of primary-Al grain along <001> direction.

432x347mm (150 x 150 DPI)

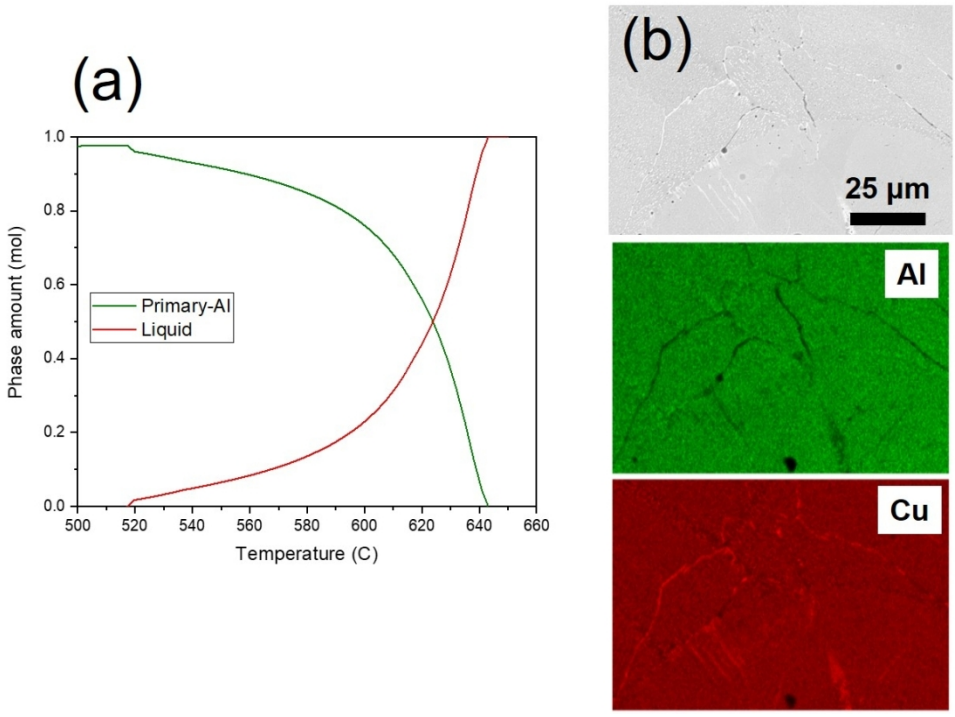

Figure 5: (a) AA2024 alloy Thermo-Calc calculated about the solidification range and (b) EDS spectra from the cracked columnar region in a sample. The grain boundary areas indicating strong segregation of Cu that is absent in the cracked regions.

214x156mm (150 x 150 DPI)

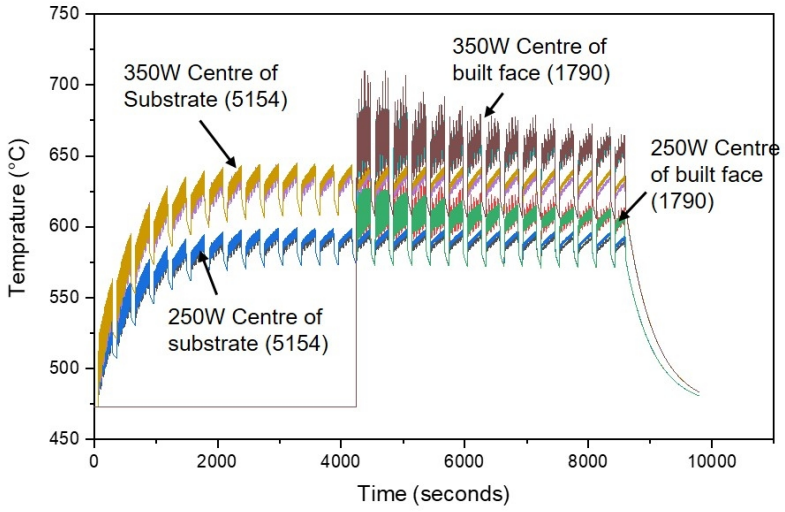

Figure 6: Abaqus predicted temperature profiles during build of 15 mm cube.

191x113mm (150 x 150 DPI)

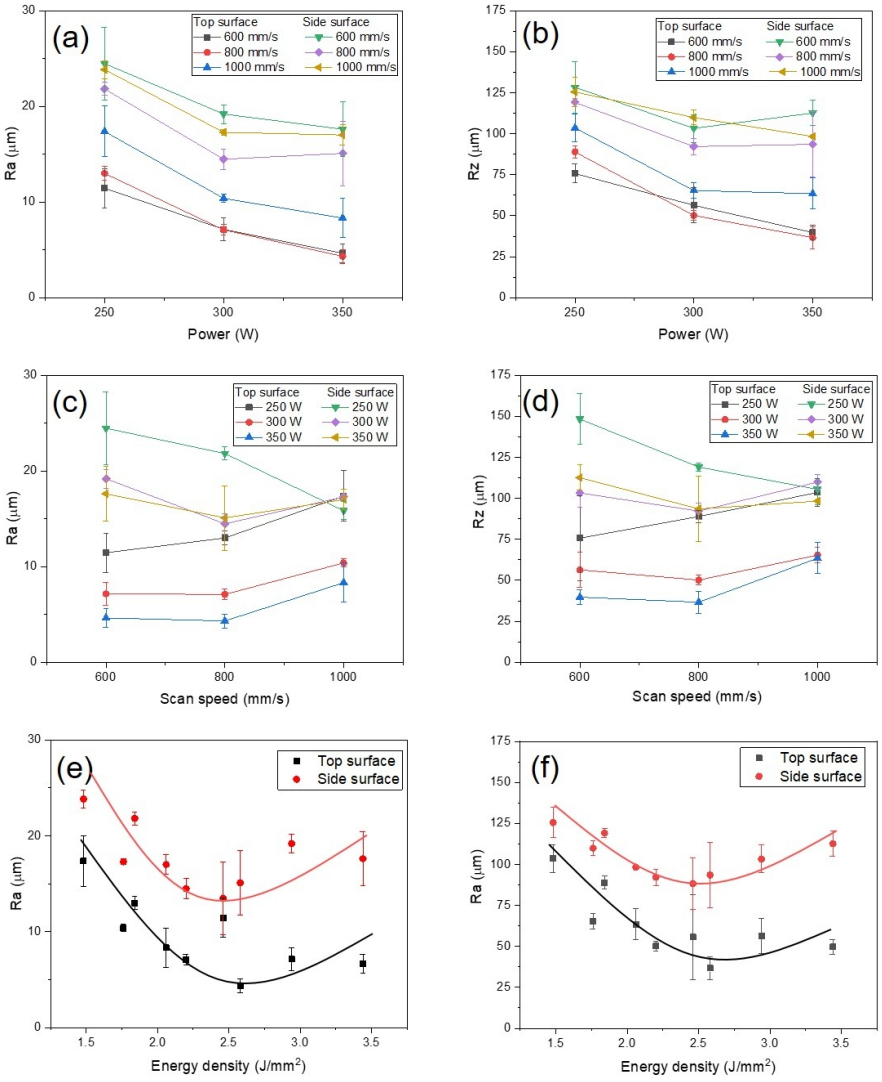

Figure 7: Variation in surface roughness of the top and side surface with (a) and (b) laser power, (c) and (d) scan speed, and (e) and (f) energy density (Ed). Ra is the average distance between the peaks and the troughs and Rz represents the vertical distance from the highest peak to the lowest trough.

207x234mm (150 x 150 DPI)

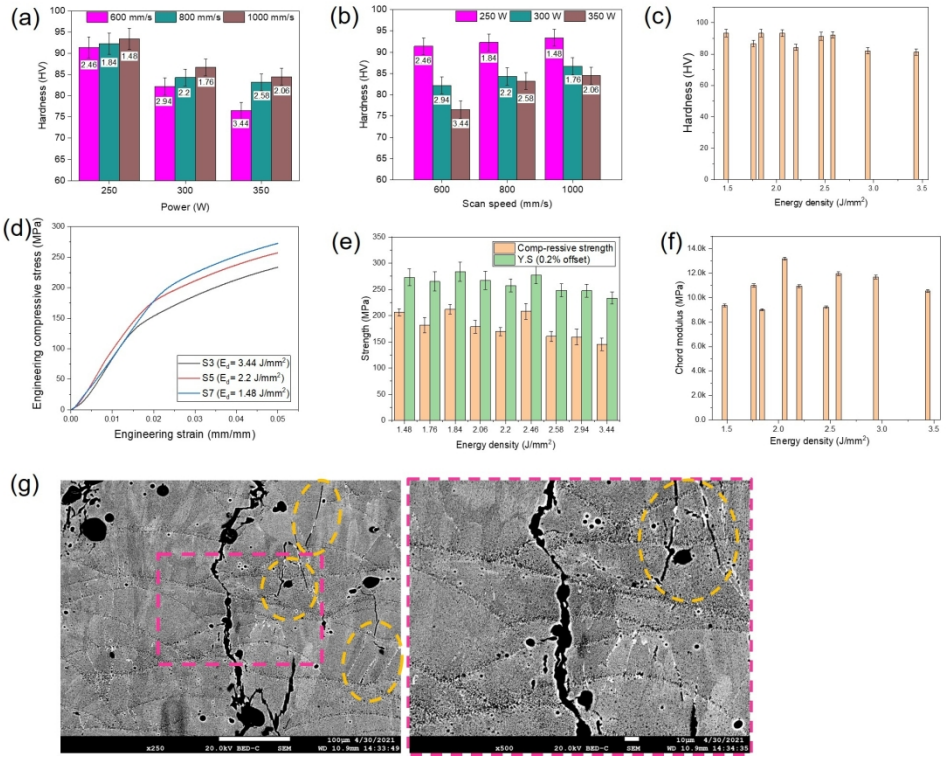

Figure 8: Microhardness of built specimen as a function of (a) laser power, (b) scan speed, and (c) energy density (Ed); Ed, is represented by the numerals in each bar of respective sample in (a) and (b). Representative engineering stress-strain curves obtained from compression testing are presented in (d), compressive strength, yield strength -0.2% off set (Y.S) and chord modules as function of Ed are presented in (e) and (f); and representative microstructure of tested sample (in build direction) shown crack opening and new cracks formation on Cu segregated grain boundary.

352x273mm (150 x 150 DPI)

Table 1. Laser parameters used for manufacturing the samples and the surface roughness of top surface and side wall of manufactured cubes.

Sample ID	**Laser power, *P* (W)**	**Scan speed, v_s (mm/s)**	**Energy density, E_d(J/mm^2)**
S1	350	1000	2.06
S2		800	2.58
S3		600	3.44
S4	300	1000	1.76
S5		800	2.2
S6		600	2.94
S7	250	1000	1.48
S8		800	1.84
S9		600	2.46